machines

MDPI

Article

Comparison of Induction Machine Drive Control Schemes on the Distribution of Power Losses in a Three-Level NPC Converter

Carlos A. Reusser [1,*,†], Matías Parra [1,†], Gerardo Mino-Aguilar [2] and Victor R. Gonzalez-Diaz [2]

[1] School of Electrical Engineering, Pontificia Universidad Católica de Valparaíso, Valparaíso 2340000, Chile; matias.parra.c@mail.pucv.cl
[2] Electronics Engineering Department, Benemérita Universidad Autónoma de Puebla, Puebla 72570, Mexico; gerardo.mino@correo.buap.mx (G.M.-A.); vicrodolfo.gonzalez@correo.buap.mx (V.R.G.-D.)
* Correspondence: carlos.reusser@pucv.cl
† These authors contributed equally to this work.

Abstract: Medium- and high-power drive applications have grown since the past decade as the most common solution for high demanding industrial processes. Multilevel converters, in particular the three-level neutral point clamped (3L-NPC) topology driving medium-voltage induction machines, has become the most commonly adopted solution. In this context, several AC drive control schemes are suitable, such as scalar control (SC), field-oriented control (FOC), model predictive control (MPC), and direct torque control (DTC). Each of these control strategies exhibit a particular operational profile which affects the switching pattern of the converter semiconductors, thus conditioning the switching and conducting losses of these power devices. This work presents a comparison of the conduction and switching losses between different drives control schemes, such as scalar control, field-oriented control, direct torque control, and model predictive control, analyzing their impact on thermal efficiency in a 3L-NPC multilevel converter, under different loading operational conditions. This analysis allows for choosing the most suitable control strategy and switching frequency for a given operational profile.

Keywords: induction machine drive; three-level NPC converter; scalar control; field-oriented control; model predictive control; direct torque control; switching losses; conduction losses; thermal efficiency

check for updates

Academic Editor: Fu-Cheng Wang

Received: 31 January 2025
Revised: 27 February 2025
Accepted: 7 March 2025
Published: 12 March 2025

Citation: Reusser, C.A.; Parra, M.; Mino-Aguilar, G.; González-Díaz, V.R. Comparison of Induction Machine Drive Control Schemes on the Distribution of Power Losses in a Three-Level NPC Converter. *Machines* **2025**, *13*, 227. https://doi.org/10.3390/machines13030227

Copyright: © 2025 by the authors. Licensee MDPI, Basel, Switzerland. This article is an open access article distributed under the terms and conditions of the Creative Commons Attribution (CC BY) license (https://creativecommons.org/licenses/by/4.0/).

1. Introduction

In the last decade, different control strategies have been developed for its application on high demanding industrial applications, such as scalar control (VF), field-oriented control (FOC), direct torque control (DTC), and model predictive control (MPC) [1–3]. Each one of these control strategies exhibit different characteristics in their torque-per-Ampere response and switching pattern, affecting the way in which each voltage vector, hence switching state, is applied in order to synthesize the required control action. This fact, which affects the semiconductor switching pattern, has a direct impact on the behavior of switching and conduction losses patterns, i.e., a modulation scheme which uses the level-shifted PWM (LS-PWM) strategy and considers symmetrical commutation between the voltage space vectors, thus producing a symmetrical switching pattern of the power semiconductors. This means that, between two switching states, only one commutation will take place. However, when using space vector modulation (SVM), without switching restrictions, it does not consider this fact, so an increase in the switching losses will take place, due to the commutation between the voltage space vectors.

Efficiency in modern power converters for high-demand industrial applications is a key design feature. In order to reduce losses and increase power density, the minimization of conduction and switching losses of power semiconductors has become a key operational factor. This implies that the power switches should be capable of working under high voltage and high switching frequency with lower losses.

The ongoing requirements for energy efficiency in power processing systems and industrial applications has encouraged the use of larger and more efficient power converters on industrial high-demand applications. Within this field of applications, multilevel voltage source converters (M-VSCs) have become the most attractive and suitable solution. Multilevel converters for drive applications have been and still continuously increase their power, leading to the need to quantify the conduction and switching losses under the action of different drive control strategies, in order to obtain a relationship between the performance of the control and the power losses of the converter and develop a decision tool for these kinds of applications.

Analysis of conduction and switching losses can be found extensively in the literature: in [4], a comparison between two-level (2L-VSC) and three-level NPC (3L-NPC) topologies is presented; in [5] a power loss calculation method is developed for its application in the 3L-NPC converters, as a function of the modulation index, power factor, and switching frequency. Also, ref. [6] proposes an approximated mathematical method to estimate the switching and conduction losses. In [7], a comparison of the converter efficiency using different modulation schemes is presented, using a linearized switching model of the converter under different operation conditions. Further research of power losses of the NPC topology is proposed in [8–10].

Power losses due to the switching and conduction profile of power semiconductors result in heat that must be dissipated from the power modules. In this context, a thermal model of the semiconductor required in order to have an approximation of the converter efficiency under different operational conditions. In this context, it should be noted that the NPC topology is known to exhibit an unequal distribution of power losses among its semiconductor devices. To mitigate the power loss imbalance in the NPC converter, the active NPC (ANPC) topology was developed [11,12].

In this paper, an analysis of the total losses in an NPC-based electric drive is presented, when using classical control schemes, such as VF, FOC, DTC, and MPC under different load conditions and switching frequencies, in order to choose the adequate control strategy and switching frequency for a given application.

The main contributions of this paper are the analysis of the total losses in an NPC-based electric drive for classical control schemes, such as VF, FOC, DTC, and MPC under different load conditions and switching frequencies and its relationship to the selection of the most suitable control strategy and switching frequency for a given operation load pattern, in terms of the impact of the system efficiency. Moreover, for particularities of the 3L-NPC topology, where the losses are unequally distributed in the active switching devices, this work offers an analysis of the life span expectations of these switching devices.

2. Converter Topology

Figure 1 shows the basic NPC cell topology, which is composed of four controlled power switches (IGBTs) with their corresponding free-wheeling diodes S_1, S_2, S_3, S_4 and two clamping diodes on each leg D_{c1}, D_{c2}.

The basic converter cell is capable of synthesizing three output voltage levels, depending on the switching states, which are summarized in Table 1.

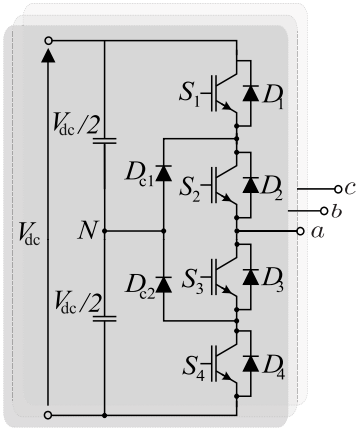

Figure 1. Three-phase NPC inverter.

Table 1. Allowable switching states of the NPC converter.

S_1	S_2	D_{c1}	V_{aN}
1	1	0	$V_{dc}/2$
0	1	1	0
0	0	0	$-V_{dc}/2$

$S_3 = \bar{S_1}$ and $S_4 = \bar{S_2}$. Considering the three-phase output voltages, the NPC converter has 27 voltage vectors which are represented in Figure 2. From these 27 voltage vectors, where 8 corresponds to redundant switching states, this means a different switching state that synthesizes the same voltage vector. According to this fact, these redundant switching states cannot be discarded when analyzing the impact in switching and conduction losses.

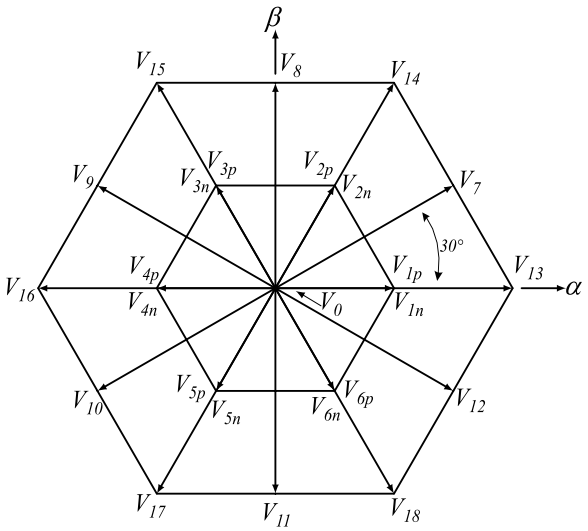

Figure 2. Space vector diagram of the NPC inverter.

As shown in Figure 2, the 27 available vector voltages can be classified into medium, large, and small vector voltages according to the following:

- Zero vector (V_0): 3 redundancies with magnitude 0.
- Small vector ($V_1 - V_6$): 2 redundancies with magnitude $V_{dc}/3$
- Medium vector ($V_7 - V_{12}$): no redundancies with magnitude equal to $\sqrt{3}V_{dc}/3$
- Large vector ($V_{13} - V_{18}$): no redundancies with magnitude equal to $2V_{dc}/3$

It should be noted that when using direct torque control and model predictive control techniques, all the vector voltages are used. This is not the case for PWM-based strategies, due the limitations introduced by the PWM modulation. In the case of the NPC converter topology, level-shifted PWM (LS-PWM) is the most commonly implemented technique, not space vector modulation (SVM), due to the complexity of the last and the restrictions in using redundancies, because of the particularities of this topology. Figure 3 shows the implementation of the LS-PWM for the 3L-NPC converter.

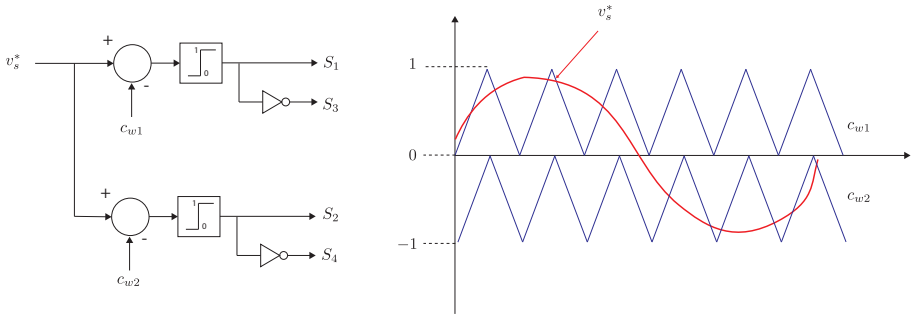

Figure 3. Level-shifted PWM implementation for a 3L-NPC converter.

3. Semiconductor Thermal Model

The key requirements for semiconductor design are achieving a high blocking voltage, low on resistance, and reliable performance at high switching frequencies. When designing semiconductors for applications such as drives, the following factors must be considered:

- Reverse recovery time;
- Rise and fall operating characteristics;
- Operating temperature.

3.1. Conduction and Switching Losses Mechanism

To accurately calculate the total power loss in an NPC converter, it is crucial to model the switching dynamics of the IGBT and its freewheeling diode, incorporating these characteristics. Figures 4–6 illustrate the typical waveforms for the on and off states of an IGBT, along with the reverse recovery time of the freewheeling diode.

Turn-on losses arise from a delay during the on-time, represented as $t_{d(on)}$. During this phase, the blocking voltage V_{dc} remains constant but decreases to a lower value during the rise time, denoted as t_r'. This voltage drop depends on the parasitic inductance L_p and the collector current i_c. Simultaneously, the current gradually increases.

An important parameter to take into account when understanding the semiconductor loss mechanism is the reverse recovery time t_{rr} of the freewheeling diode. Before commutation, the current flows through the diode and then transitions to the IGBT after turning on. Due to the diode's reverse recovery behavior, a current overshoot occurs, leading to a peak of power, as shown in Figure 4. Once t_{rr} passes, the voltage reduces to its nominal value V_{ces}, resulting in the consequent conduction losses.

The off-time waveforms of the IGBT behavior are illustrated in Figure 5. The on-voltage in the IGBT V_{ces}, increases until it reaches the blocking voltage, V_{dc}. The change in voltage can be considered linear. The voltage waveform exhibits underdamped characteristics with an overshoot due to the parasitic inductance, L_p. The current through the IGBT decreases rapidly and transfers to the freewheeling diode. Additionally, the rapid change in current explains the peak voltage during the commutation and the peak power value.

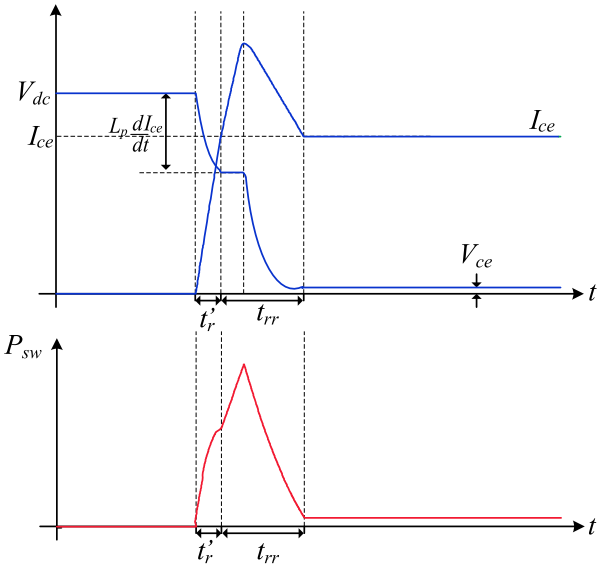

Figure 4. Switching wave forms in the turn-on time.

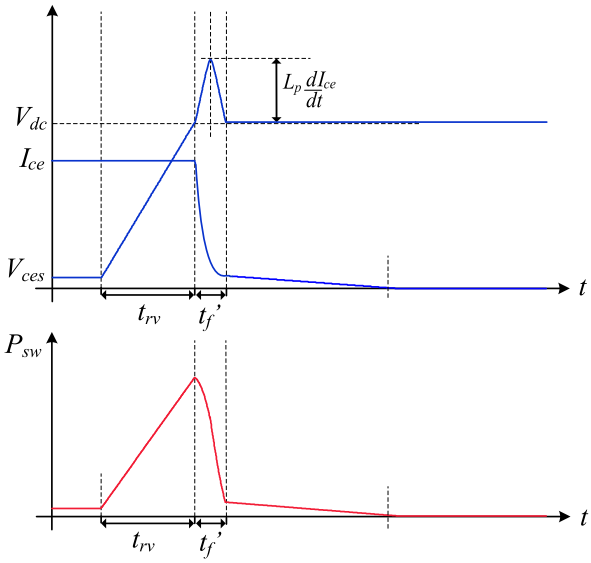

Figure 5. Switching wave forms in the turn-off time.

During the turn-off phase of the freewheeling diode, as illustrated in Figure 6, the reverse recovery effect becomes evident. Initially, the diode current decreases linearly until it reaches a negative peak value. When the current turns negative and continues to increase, this duration is referred to as t_{rra} (reverse recovery active time) during which the diode remains in the conducting state. After t_{rra}, the current begins to rise linearly until the diode becomes fully blocked at time t_{rrb} (reverse recovery blocking time). Throughout t_{rrb}, the current decreases while the voltage V_{ce} falls, describing the reverse recovery characteristics of the diode. During t_{rrb}, the current and voltage increase until the diode reaches its blocking state, resulting in power loss. This phenomenon is referred to as the reverse recovery charge [4].

With the switching behavior established, the IGBT's dynamics can be categorized into two primary losses mechanisms: switching losses and conduction losses. Since the diode exhibits similar dynamic behavior to the IGBT, its detailed analysis is omitted.

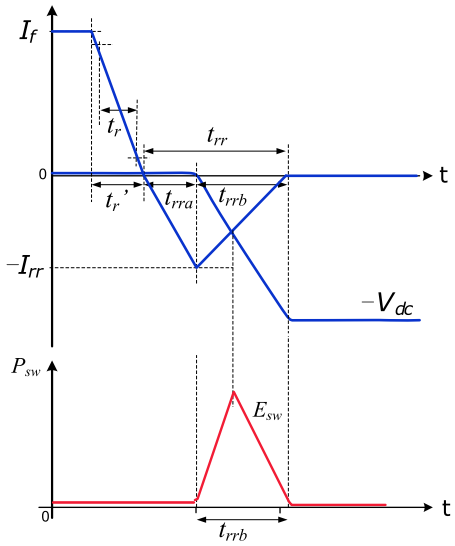

Figure 6. Reverse recovery time of the freewheeling diode.

3.2. Conduction Loss Calculation

Because of the almost linear behavior of conduction losses, as described previously, which can be characterized as an on-resistance r_{ce}, conduction loss calculation can be defined as the power dissipated due to the current flowing through the semiconductor's on-resistance, when the switch is on its on state. It should be noted that these losses depend on the current drawn by the load, depending on the operational condition. Power loss calculation can be summarized as follows:

$$P_{cond} = D\left(v_{ce}\, i_{c,med} + r_{ce}\, i_{c,rms}^2\right) \tag{1}$$

where D is the duty cycle, $i_{c,med}$ and $i_{c,rms}$ stand for the mean and rms value of the load flowing through the semiconductor respectively, r_{ce} is the internal on-resistance, and v_{ce} is the semiconductor's on-voltage . The duty cycle dependence of conduction losses, reflected in the need of $i_{c,med}$, makes its calculation more complex due to the implementation of a PWM modulation scheme, making $i_{c,med}$ highly dependent on the modulation index and carrier wave frequency.

Due to this complexity, the estimation of conduction losses is obtained using PLECS v.4.9 software and the semiconductor models, configured with the device characteristic curves, provided by the manufacturer data-sheet.

Figure 7 shows the collector current as a function of the collector–emitter voltage ($I_c = f(V_{ce})$). The conduction behavior is tested at different temperatures and gate voltages. These characteristics are introduced into the PLECS model for the conduction loss calculations.

3.3. Switching Loss Calculation

Switching losses can be separated into two stages: the on-time and the off-time. As explained previously, these losses are due to effect of the parasitic inductance L_p, the reverse recovery time of the freewheeling diode t_{rr}, and the switching frequency. So they can be understood as the rate of change in the stored energy in the semiconductor's parasitic inductance and calculated as follows:

$$P_{sw} = \frac{1}{\pi} f_s \left(E_{on}(i) + E_{off}(i)\right) \tag{2}$$

The switching losses depend directly on the switching frequency but also on the on and off energy. This energy is a function of the collector current and is represented by characteristic curves in the data-sheet of the semiconductor, shown in the Figure 8.

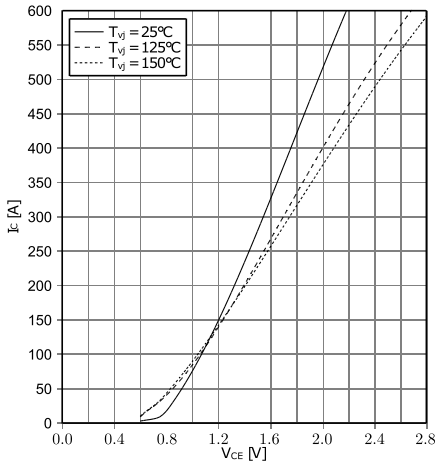

Figure 7. Collector current v/s collector–emitter voltage.

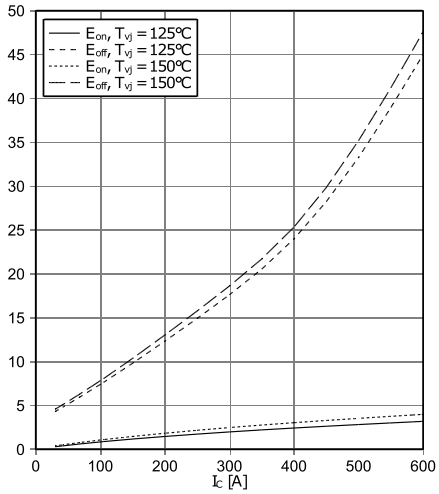

Figure 8. On and off energy characteristics.

If the converter, for a given delivered power, operates at a high switching frequency, the power losses will increase with respect to the conduction losses, resulting in a decrease in system performance.

$$\eta = 1 - \frac{P_{cond} + P_{sw}}{P_{in}} \tag{3}$$

In (3), it shows the relationship between the efficiency of the drive and the power losses in the converter. If the converter operates at a high switching frequency, the efficiency will be low. The frequency that defines the limit where switching losses dominate over conduction losses is referred to as the critical frequency .

In Figure 9, the behavior of the converter efficiency and the switching frequency is shown. Below the critical frequency, the power losses of the converter are dominated by conduction losses, and the efficiency will depend directly on the load. However, if the operating frequency exceeds the critical frequency, the power losses will be dominated by switching losses, and the efficiency will be affected accordingly.

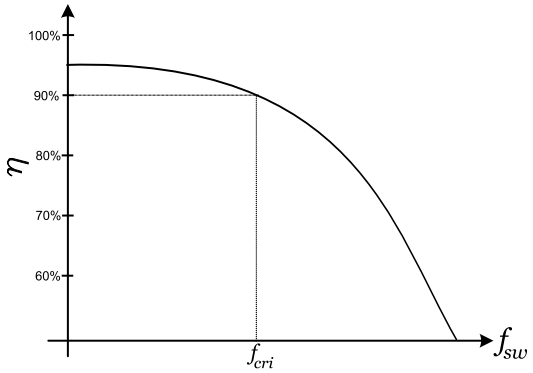

Figure 9. Relationship between the switching frequency and the efficiency of the converter.

3.4. Thermal Model

Switching and conduction power losses result in heat, which has to be transferred internally from the semiconductor to the environment through a heat sink. However, there are different layers to be taken into account between the semiconductor itself and the heat sink. Figures 10 and 11 show the schematic of the heat transfer model, considering the different layers involved in this process [13].

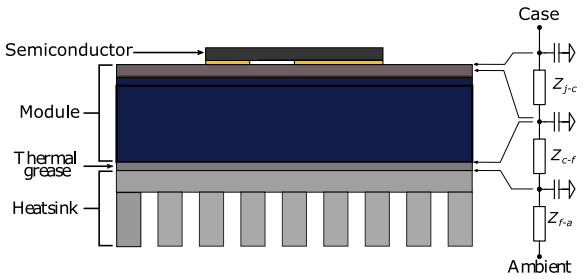

Figure 10. Thermal model of a semiconductor.

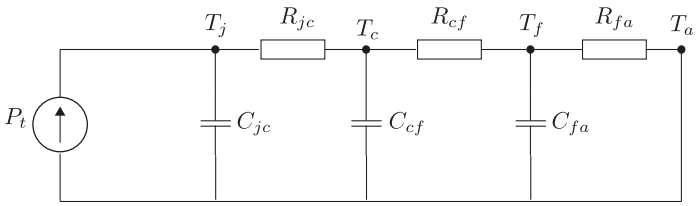

Figure 11. Equivalent thermal model of the semiconductor.

The thermal capacity C_{jk} (e.g., C_{jc} junction to case, C_{cf} case to heat sink, and C_{fa} heat sink to ambient) and thermal resistance R_{jk} (e.g., R_{jc} junction to case, R_{cf} case to heat sink, and R_{fa} heat sink to ambient) are defined by the manufacturer and can be modeled as a capacitor and a resistor, respectively, as follows:

$$z_{jk}(t) = \sum_{i=1}^{N} R_i \left(1 - e^{-t/\tau_i}\right) \tag{4}$$

where τ_i stands for the thermal transient and is defined as follows in Equation (5):

$$\tau_i = R_i C_i \tag{5}$$

Due to the heat and the different materials used, the thermal impedance for each different layer will have specific values provided by the manufacturer, specifically, Z_{jc} for junction to the case of thermal impedance, the Z_{cf} case to heat sink thermal impedance, and Z_{fa} heat sink to ambient thermal impedance, as shown in Figure 11.

Figure 12 shows the losses and thermal equivalent model of the IGBT used in PLECS. The software is capable of simulating the switching and conduction behavior curves at different operating temperatures. Additionally, using the data provided by the manufacturer, it is possible to simulate the equivalent thermal circuit.

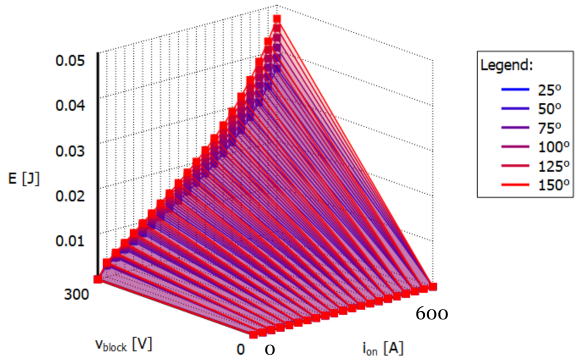

Figure 12. Semiconductor model in PLECS.

For this work, an F3L300R07PE4 IGBT, NPC Infineon module [14] was chosen for its application on a 15 [kW] induction machine drive. All the switching and conduction characteristic curves were integrated in the PLECS simulation component provided by Infineon. This device is recommended for its application on electric drives, considering a DC link voltage of $V_{dc} = 600$ [V], a maximum blocking voltage of 300 [V], and a suitable collector current $I_c = 300$ [A] capable of handling a starting current of 5 to 9 times the nominal current of the driving machine.

4. Induction Machine Dynamic Model

The dynamical model of the electric drive, in this case, a squirrel cage induction machine, is defined by the corresponding stator and rotor dynamics, represented in the stationary $\alpha\beta$ reference frame.

$$v_s^{\alpha\beta} = R_s\, i_s^{\alpha\beta} + \frac{d}{dt}\psi_s^{\alpha\beta} \tag{6}$$

$$0 = R_r\, i_r^{\alpha\beta} + \frac{d}{dt}\psi_r^{\alpha\beta} - jp\omega_r\, \psi_r^{\alpha\beta} \tag{7}$$

where $\psi_s^{\alpha\beta}$ and $\psi_r^{\alpha\beta}$ are the stator and rotor flux linkage, respectively, and p the pole pairs. The flux linkages are defined in Equations (8) and (9):

$$\psi_s^{\alpha\beta} = L_s\, i_s^{\alpha\beta} + L_m\, i_r^{\alpha\beta} \tag{8}$$

$$\psi_r^{\alpha\beta} = L_r\, i_r^{\alpha\beta} + L_m\, i_s^{\alpha\beta} \tag{9}$$

Replacing (8) and (9) into Equations (6) and (7) leads to the dynamic model in stator currents and rotor flux linkage state variables y in the $\alpha\ \beta$ stationary reference frame.

$$\tau_\sigma \frac{d}{dt} i_s^{\alpha\beta} + i_s^{\alpha\beta} = \frac{1}{R_\sigma} v_s^{\alpha\beta} + \frac{L_m}{R_\sigma L_\sigma \tau_r} \psi_r^{\alpha\beta} - j\frac{L_m}{R_\sigma L_r} p\omega_r \psi_r^{\alpha\beta} \tag{10}$$

$$\tau_r \frac{d}{dt} \psi_r^{\alpha\beta} + \psi_r^{\alpha\beta} = L_m\, i_s^{\alpha\beta} + j\, p\omega_r\, \tau_r \psi_r^{\alpha\beta} \tag{11}$$

where $\tau_r = L_r / R_r$ is the rotor time constant; ω_k is the synchronous speed; p is the number of pole pairs; ω_r is the mechanical rotor speed; $\tau_\sigma = \sigma L_s / R_\sigma$ is the stator time constant; σ is the dispersion factor; and ω_{sl} is the slip speed.

By rotating Equations (10) and (11) into the dq synchronous reference frame by means of the unitary rotation matrix U in Equation (12), the dynamic model of the induction machine in dq synchronous coordinates is obtained, as described in Equations (13) and (14):

$$U = \begin{bmatrix} \cos\theta_k & \sin\theta_k \\ -\sin\theta_k & \cos\theta_k \end{bmatrix} \tag{12}$$

$$\tau_\sigma \frac{di_s^{dq}}{dt} + i_s^{dq} = \frac{1}{R_\sigma} v_s^{dq} + \frac{L_m}{R_\sigma L_r \tau_r} \psi_r^{dq} - \frac{L_m}{R_\sigma L_r} jp\omega_r \psi_r^{dq} - j\omega_k \tau_\sigma i_s^{dq} \tag{13}$$

$$\tau_r \frac{\psi_r^{dq}}{dt} + \psi_r^{dq} = L_m i_s^{dq} - \tau_r j\omega_{sl} \psi_r^{dq} \tag{14}$$

The electrical torque by the induction machine in the dq reference frame is given via Equation (15):

$$T_e = \frac{3}{2} p \frac{L_m}{L_r} \left[\psi_r^d \, i_s^q - \psi_r^q \, i_s^d \right] \tag{15}$$

Finally, the mechanical dynamic is defined by Equation (16) as follows:

$$J \frac{d}{dt} \omega_r = T_e - T_L \tag{16}$$

where J is the machine inertia, and T_L is the load torque.

5. Control Schemes

5.1. Scalar Control

Scalar control (SC) and vector control are the primary methods used for controlling induction machines. The latter can be implemented through either direct torque control (DTC) or field-oriented control (FOC) techniques. Scalar control offers several advantages over DTC and FOC, including simplicity on its implementation, simple architecture, high cost-effectiveness ratio, and no dependence on system parameters for controller tuning (when operating in a closed-loop configuration).

Its operation principle is based on varying the voltage and frequency, thus maintaining the same voltage-to-frequency ratio [2]. This constant V-f ratio ensures the operation with constant flux linkage and, hence, provides constant torque operation over a certain speed range, which is defined in three different regions. First, voltage drop compensation region, which is the low-frequency region starting at frequency $f_k = 0$ [Hz], where a constant voltage V_{min} is required to overcome the voltage drop in stator impedance; the upper frequency limit f_{min} of this region depends on the characteristics of the machine. Second, the constant torque region, in which the voltage to frequency ratio is maintained constant as explained previously with an upper limit that corresponds to the rated frequency f_{rat}. Finally, the saturation region, in which, when going into frequencies above f_{rat}, the converter output voltage remains constant to its maximum modulation index corresponding to the drive's rated voltage V_{rat}, because of the saturation of the output voltage the electric drive operates in field weakening condition. Figure 13 shows the corresponding voltage to frequency operation characteristic of a scalar control scheme. The closed-loop SC control scheme is based on a single-speed feed-back control loop, as shown in Figure 14.

The torque control action is based on a linear approximation of the stationary torque characteristic of the IM, when considering the machine operating close to the nominal slip, under constant voltage-to-frequency ratios, for a given frequency. Within this operational range, the torque characteristic can be approximated as Equation (17):

$$T_e = K_v \, \psi_{rat}^2 \, \omega_{sl} \tag{17}$$

where K_v is a constant depending on the machine's parameters. As shown in Figure 14 and from Equation (17), the PI controller control actuation corresponds to the rotational speed reference ω_{sl}^*. To obtain the desired synchronous speed reference to be synthesized, the actual rotational speed ω_r converted to electrical variable is added as follows:

$$\omega_e^* = \omega_{sl}^* + p\,\omega_r \tag{18}$$

The synchronous frequency ω_e^* is used to synthesize the respective sinusoidal references, considering the V-f characteristic. The main drawbacks of this control scheme can be found as follows: poor dynamic performance due to the coupling effect of the mechanical and electrical dynamics; high slip beyond the nominal slip operation leading to poor power factor control; low efficiency in the voltage drop compensation region due to the increase in voltage drop losses; and lack of control capability in the field weakening region.

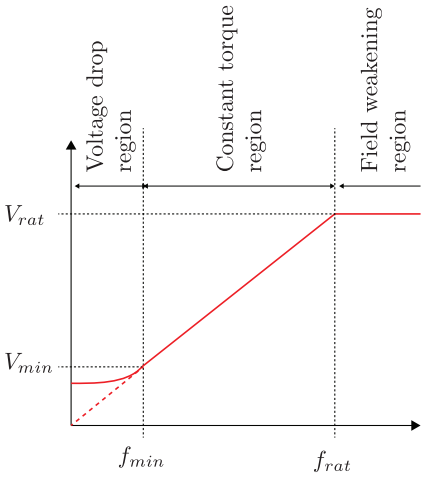

Figure 13. Voltage-to-frequency characteristic.

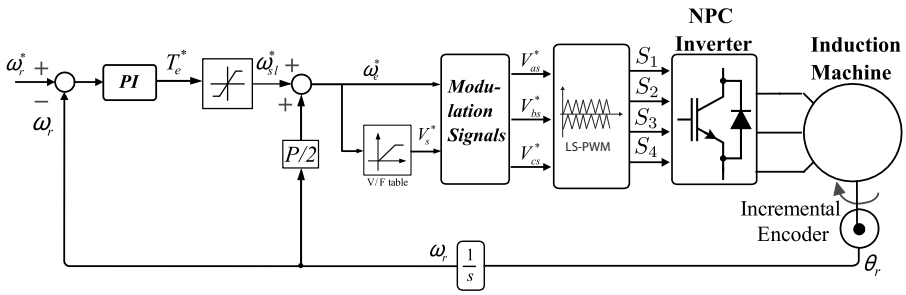

Figure 14. Block diagram of scalar control.

5.2. Field-Oriented Control

Field-oriented control is a linear control technique in which the state space variables are rotated into the dq asynchronous reference frame by means of the rotation matrix in Equation (12); the rotation angle θ_k is selected in such a way that it is possible to decouple the stator current state variable into two orthogonal components; one related to the torque and the other to the production of the flux linkage [2]. If the rotation angle θ_k is selected such that it is fixed to the rotor flux linkage state space vector ψ_r, the corresponding dq components hence became: $\psi_r^d = |\psi_r|$ and $\psi_r^q = 0$, so the torque relationship given in Equation (15) is reduced to the following:

$$T_e = \frac{3}{2} p \frac{L_m}{L_r} |\psi_r|\, i_s^q \tag{19}$$

On the other hand, Equation (14) in steady state is reduced to the following:

$$|\psi_r| = L_m\, i_s^d \tag{20}$$

Equations (19) and (20) state that the torque is controlled by i_s^q and the rotor flux linkage by means of controlling i_s^d, so the torque and field may be controlled independently. This means that optimum torque will be achieved by ensuring nominal flux, also in zero speed. The speed control loop, is designed as a cascaded outer loop, as shown in Figure 15, and linear controllers are designed in such a way that the dynamics of inner and outer control loops are perfectly decoupled.

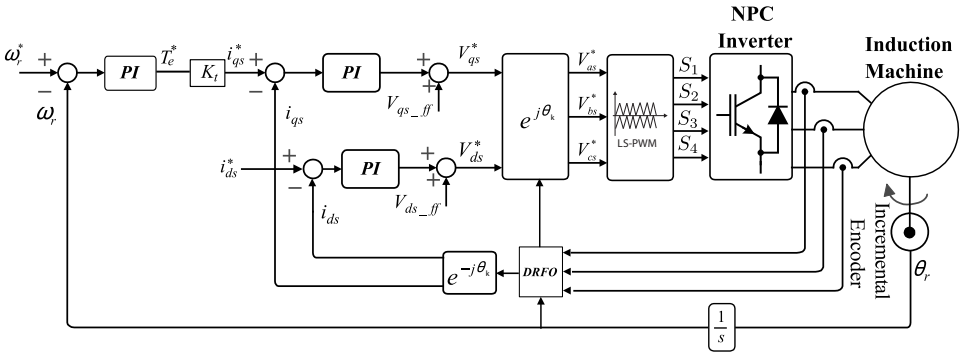

Figure 15. Block diagram of field-oriented control.

Because it is not possible to directly measure the rotor flux state variable, it is necessary to design a rotor flux estimator structure to extract the synchronous angle θ_k and properly rotate the measured stator currents into the dq synchronous reference frame. Although there are several open-loop and closed-loop estimation structures, the most commonly used is the direct reference frame orientation (DRFO) technique based on a current model structure [15,16].

The current model based DRFO estimates the rotor flux linkage in the $\alpha\,\beta$ stationary reference frame directly using Equation (11). However, the implementation of the current model used in the $\alpha\beta$ stationary reference frame could lead to computational overflow. One solution is to rotate Equation (11) into the xy reference frame, which is solitary to the rotor, thus transforming to Equation (21) as follows:

$$\tau_r \frac{d}{dt}\psi_r^{xy} + \psi_r^{xy} = L_m\, i_s^{xy} \tag{21}$$

$$\psi_r^{\alpha\beta} = \psi_r^{xy}\, e^{jp\theta_r} \tag{22}$$

$$\theta_k = \arctan 2\left(\frac{\psi_r^{\beta}}{\psi_r^{\alpha}}\right) \tag{23}$$

It should be noted that the rotor position θ_r is needed to obtain the estimated rotor flux linkage state variable, hence the synchronous angle θ_k. Figure 16 shows the block diagram for this structure.

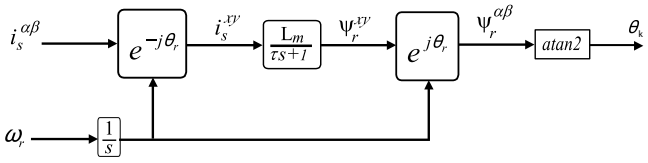

Figure 16. Current model DRFO structure.

Field-oriented control is a very well-known technique, used in a wide range of heavy-duty industrial applications, mainly due to its main features of decoupled torque and field control, which enables the electric drive to exhibit high efficiency in the constant field and field weakening regions. Because it is a PWM control technique, the harmonic content is constrained to the carrier-wave frequency; hence, current harmonics are also constrained to a low THD, as well as the torque harmonic components.

The main drawbacks of this strategy are the bandwidth limitations of the PI controllers; the necessity of a anti-windup scheme because of the cascaded control loop; the need for feed-forward compensation for the inner-loop controllers because of the internal disturbances assigned to the non-linearity; and finally, the dependence on system parameters, especially in the design and correct operation of the flux estimator loop. The correct orientation is fundamental for the performance of the electric drive.

5.3. Direct Torque Control

Direct torque control is a non-linear control strategy, based on applying different switching states on the power converter, to control torques and fields based on hysteresis controllers. In this regard, the electricity defined in Equation (16), expressed in terms of the stator and rotor flux linkage state variables, becomes the following:

$$T_e = \frac{3\,p\,L_m}{\sigma\,L_s\,L_r}\,|\psi_s|\,|\psi_r|\,sin(\theta_{rs}) \tag{24}$$

where θ_{rs} is the angle between the rotor and stator flux. Equation (24) corresponds to the cross product of both stator and rotor flux linkages, hence the electromagnetic torque developed by the machine. The stator flux can be obtained in Equation (6) as follows:

$$\frac{d}{dt}\psi_s^{\alpha\beta} = v_s^{\alpha\beta} - R_s\,i_s^{\alpha\beta} \tag{25}$$

By considering that this control strategy is based on the application of a finite set of discrete switching states, and neglecting the effect of stator resistance R_s, the dynamics of (25) can be represented by the Euler approximation, as shown in Equation (26):

$$\psi_s^{\alpha\beta}[k+1] = \psi_s^{\alpha\beta}[k] + T_s\,v_s^{\alpha\beta}[k] \tag{26}$$

Equation (26) states that it is possible to predict the stator flux linkage state at sample $k+1$, $\psi_s^{\alpha\beta}[k+1]$, given the actual state $\psi_s^{\alpha\beta}[k]$ and the input voltage vector $v_s^{\alpha\beta}[k]$, which is dependent on a finite set of switching sates. So, the amplitude and phase of $\psi_s^{\alpha\beta}[k+1]$ depend on the switching state and the space vector sector on which it exists in sample k. The corresponding space vector sectors for the NPC converter are shown in Figure 17.

It can be considered that the rotor flux linkage stays invariant between samples due to the fact that, generally, $\tau_r \gg \tau_s$ [3], so if the sample time T_s is sufficiently small, then Equation (24) can be expressed as follows:

$$T_e = K\,|\psi_s^{\alpha\beta}[k+1]|\,sin(\theta_{rs}[k+1]) \tag{27}$$

Hysteresis controllers are used for torque and field control, defining x_T and x_ψ as the torque and stator flux control actuation, which are preset to increase/decrease the torque and flux, respectively. For the NPC converter, a five-level hysteresis control was considered for torque control [17] to allow for the utilization of medium and large vector voltages, thereby enhancing the performance of the torque controller.

$$x_T = \begin{cases} 2 & ; \quad T_{err} \geq \Delta T_e \\ 1 & ; \quad \Delta T_e/2 \leq T_{err} < \Delta T_e \\ 0 & ; \quad -\Delta T_e/2 \leq T_{err} < \Delta T_e/2 \\ -1 & ; \quad -\Delta T_e \leq T_{err} < -\Delta T_e/2 \\ -2 & ; \quad T_{err} < -\Delta T_e \end{cases} \tag{28}$$

where T_{err} stands for the torque error between the estimated torque and the torque reference and ΔT_e for the hysteresis band width. In the case of the stator field control, a single hysteresis band is sufficient since the stator flux reference remains constant at its nominal value.

$$x_\psi = \begin{cases} 1 & ; \quad \psi_{err} \geq \Delta\psi \\ 0 & ; \quad \psi_{err} < -\Delta\psi \end{cases} \tag{29}$$

where ψ_{err} stands for the torque error between the estimated stator flux linkage and the reference value, and $\Delta\psi$ stands for the hysteresis band width. Table 2 summarizes the corresponding switching state for each space vector sector, according to x_T and x_ψ [1].

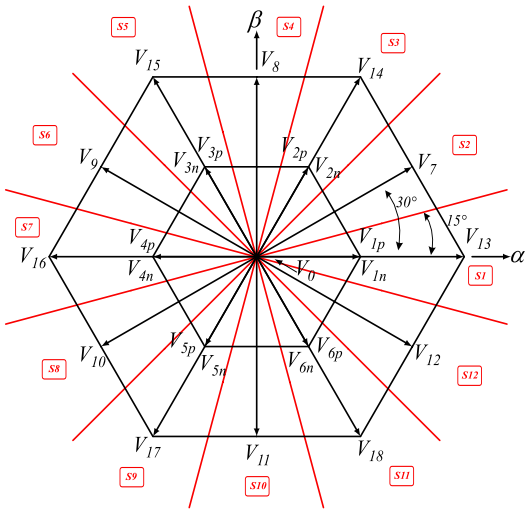

Figure 17. DTC space vector sector diagram for the 3L-NPC topology.

Table 2. Switching logic table for a 3L-NPC topology.

x_ψ	x_T	S.1	S.2	S.3	S.4	S.5	S.6	S.7	S.8	S.9	S.10	S.11	S.12
1	2	V_{15}	V_9	V_{16}	V_{10}	V_{17}	V_{11}	V_{18}	V_{12}	V_{13}	V_7	V_{14}	V_8
	1	V_3	V_3	V_4	V_4	V_5	V_5	V_6	V_6	V_1	V_1	V_2	V_2
	0	V_0	V_0	V_0	V_0	V_0	V_0	V_0	V_0	V_0	V_0	V_0	V_0
	−1	V_6	V_6	V_1	V_1	V_2	V_2	V_3	V_3	V_4	V_4	V_5	V_5
	−2	V_{11}	V_{18}	V_{12}	V_{13}	V_7	V_{14}	V_8	V_{15}	V_9	V_{16}	V_{10}	V_{17}
0	2	V_{14}	V_8	V_{15}	V_9	V_{16}	V_{10}	V_{17}	V_{11}	V_{18}	V_{12}	V_{13}	V_7
	1	V_2	V_2	V_3	V_3	V_4	V_4	V_5	V_5	V_6	V_6	V_1	V_1
	0	V_0	V_0	V_0	V_0	V_0	V_0	V_0	V_0	V_0	V_0	V_0	V_0
	−1	V_1	V_1	V_2	V_2	V_3	V_3	V_4	V_4	V_5	V_5	V_6	V_6
	−2	V_{12}	V_{13}	V_7	V_{14}	V_8	V_{15}	V_9	V_{16}	V_{10}	V_{17}	V_{11}	V_{18}

As in the case of FOC, in DTC, it is required to estimate the stator flux linkage state space variable and the electromechanical torque. The stator flux linkage estimator is obtained by expressing $i_r^{\alpha\beta}$ on Equation (9) in terms of $\psi_s^{\alpha\beta}$ and $i_s^{\alpha\beta}$ and substituting into Equation (8), thus yielding the following:

$$\psi_s^{\alpha\beta} = \frac{L_m}{L_r}\,\psi_r^{\alpha\beta} + \sigma\, L_s\, i_s^{\alpha\beta} \tag{30}$$

Here, the rotor flux linkage state variable $\psi_r^{\alpha\beta}$ is estimated from a DRFO current model structure as presented previously in Equations (21)–(23)

The torque estimation can be derived from Equation (15) in terms of $\psi_s^{\alpha\beta}$ and $i_s^{\alpha\beta}$ state variables as follows:

$$T_e = \frac{3}{2} p \left[\psi_s^{\alpha} \, i_s^{\beta} - \psi_s^{\beta} \, i_s^{\alpha} \right] \tag{31}$$

where $\psi_s^{\alpha\beta}$ is obtained from the flux estimator defined in Equation (30).

Implementation of the DTC control scheme is shown in Figure 18. The main advantages of this control technique are related to the rapid response of the hysteresis controllers, which does not overshoot, making it a very attractive control strategy for applications where high precision and fast responses are required. On the other hand, in terms of achieving high performance, the complexity of the switching tables to be implemented increases dramatically when considering multilevel converter topologies. Also, because the switching frequency is variable (depends on the switching table), there is significant torque and flux ripple build-up.

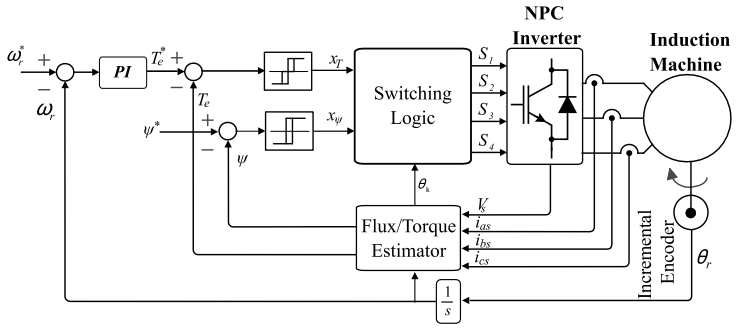

Figure 18. Block diagram of the DTC control scheme.

5.4. Model Predictive Control

Model predictive control (MPC) has gained significant popularity for its application in electric drives. This is primarily due to its intuitive concept, fast dynamic response, simple computational implementation, and the fact that it doesn't require a complex cascaded control scheme, as the case of FOC and DTC [1,18,19]. Additional benefits include flexibility, rapid response times, ease of constraint handling, and the ability to handle multiple objectives. This allows for an added degree of freedom by incorporating frequency switching constrains within a single cost function. The prediction model is derived by discretizing the dynamic model of the IM described in Equations (13) and (14) by using Euler approximation.

$$\begin{aligned} i_s^{dq}[k+1,i] = \left(1 - \frac{T_s \, R_s}{\sigma \, L_s}\right) i_s^{dq}[k] + \frac{T_s \, L_m}{R_\sigma L_r \tau_r} \psi_r^{dq}[k] - \frac{T_s \, L_m}{R_\sigma L_r} j \, p \, \omega_r \, \psi_r^{dq}[k] \\ - j \, T_s \, \omega_k \tau_\sigma i_s^{dq}[k] + \frac{T_s}{\sigma \, L_s} v_s^{dq}[k,i] \end{aligned} \tag{32}$$

$$\psi_r^{dq}[k+1] = \left(1 - \frac{T_s}{\tau_r}\right) \psi_r^{dq}[k] + \frac{L_m}{\tau_r} i_s^{dq}[k] - j\omega_{sl} \psi_r^{dq}[k] \tag{33}$$

Here, $i_s^{dq}[k+1,i]$ stands for the prediction of the current state space variable, given the i voltage vector applied (in the case of the NPC converter, as described previously, there are 27 voltage vectors). The cost function is defined as the quadratic error of the stator current

and the rotor flux linkage, as well as state space variables, as shown in Equation (34) for $i = [1 \dots 27]$ as follows:

$$g(i) = \lambda_1 \left(i_s^{*dq} - i_s^{dq}[k+1, i] \right)^2 + \lambda_2 \left(\psi_r^{*dq} - \psi_r^{dq}[k+1] \right)^2 \tag{34}$$

The optimization objective $\mathcal{O}$ is expressed as follows:

$$\mathcal{O} = \min\{g(i)\} \tag{35}$$

The overall control scheme is illustrated in Figure 19.

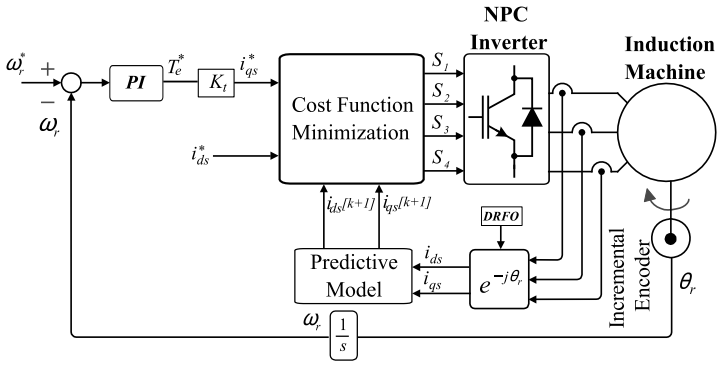

Figure 19. Block diagram of model predictive control.

Unlike conventional control strategies, which include a modulation technique to regulate the switching frequency of the semiconductors, MPC does not account for this aspect because, as in the case of DTC, the switching state is selected from the minimization of the cost function. Although there are various methods to impose a limit on switching frequency [20–22], this study adopts a different approach by penalizing the cost function using a Notch filter [23]. The filter accounts for the control loop error within the cost functional outlined in Equation (34). It modifies the cost function to assign high values at both low and high frequencies while significantly reducing the value at the target frequency ω, as shown in Equation (36) as follows:

$$G_f(i) = |H_f| g(i) \tag{36}$$

So the optimization target is now defined as follows:

$$\mathcal{O} = \min\left\{ G_f(i) \right\} \tag{37}$$

This approach helps us to avoid voltage vectors that would lead to excessively high switching frequencies at the desired operating frequency. In essence, the filter behaves similarly to a resonance filter near the desired frequency. The structure of the discrete Notch filter is presented in Equation (38) as follows:

$$H_f = \frac{z^2 - 2\cos\omega\, z + 1}{z^2 - 2a\cos\omega\, z + a^2} \tag{38}$$

The response of the Notch filter in terms of the switching frequency ω_s and the desired frequency ω will be as follows:

$$|H_f| = \begin{cases} \infty & ; \omega_s \neq \omega \\ 0 & ; \omega_s = \omega \end{cases} \tag{39}$$

6. Results

The results were obtained using a hardware-in-the-loop (HIL) setup, based on an RT-Box-3 platform and a LaunchPad interface, as shown in Figure 20. Modulation and drive control schemes were implemented in an external TI C2000 micro-controller provided with the Plexim RT-Box LaunchPad interface integrated to the launchpad interface, while the converter topology and the AC-drive ran in a real-time simulation. Waveforms of the interested system variables were routed out using the RT-Box LaunchPad interface and plotted into an oscilloscope.

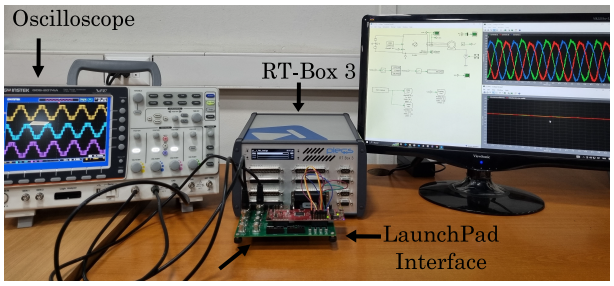

Figure 20. HIL-based validation setup.

For a correct power analysis, the setting of the operational conditions for each control scheme were the same: speed reference is defined at the rated speed and the torque reference was increased in steps of 25% from his nominal value until the rated torque.

The parameters used for real-time simulation are presented in Table 3. It should be noted that the DC link voltage is set to 600 V, so common mode injection for the sinusoidal pulse width modulation (SPWM) technique has been implemented. Additionally, the peak starting current of the IM drive is specified up to seven times its nominal current, and the chosen value for $I_{c,nom}$ is even higher, indicating no issues with the semiconductor components.

For the calculation of the power losses, a sub-cell of the the fundamental cell has been considered, consisting of a symmetric semiconductor arrangement, e.g., semiconductors S_1, D_1, S_2, D_2, and D_{c1} (refer to Figure 1). In this regard, the total converter losses were calculated as six times the sub-cell losses. Figure 21 shows the power losses of each semiconductor device of sub-cell configuration referred previously. It should be noted that the SPWM implemented in the case of SC and FOC control techniques works with a carrier wave signal of 5 kHz.

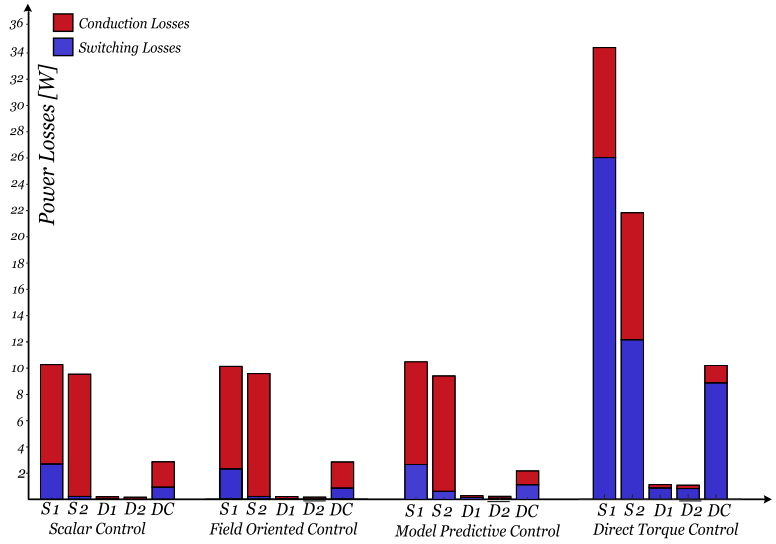

Figure 21. Power losses of each semiconductor (rated load).

As presented in Figure 21, independent of the control strategy, power losses are concentrated in S_1 and S_2 devices, while losses in D_1 and D_2 have a negligible contribution to losses. On the other hand, losses on clamping devices D_{c1} will depend on the control strategy; SC, FOC, and MPC (with the limitation of switching frequency) exhibit similar amount of total losses, while, DTC exhibits the highest losses, comparable to the losses of the switching devices S_1 and S_2 in SC, FOC, and MPC schemes.

When comparing the switching and conduction losses of SC, FOC, and MPC schemes, the results are quite similar. In this context, it should be noted that, in the MPC control strategy, the switching frequency has been penalized in the cost function, thus forcing the algorithm to work in the bounding of the fixed switched frequency of SC and FOC schemes. Concurrently, switching losses are considerably decreased. In this context, the similarity, in the distribution of power losses between SC and FOC, can be attributed to both control schemes that are based on the use of sinusoidal pulse width modulation (SPWM).

DTC, on the other hand, exhibits higher switching losses when compared to SC, FOC, and MPC with frequency limitations. This fact is because of the non-dependence on the switching frequency, in the switching state selection given by the hysteresis controller and the switching table. In other words, the selected switching state is imposed in a variable period of time, unlike SPWM-based control strategies, where each switching state is applied in a fixed time period, with respect to the sampling time (duty cycle), which depends on the amplitude of the voltage to be synthesized, using the power converter. At the same time, conduction losses for the DTC control scheme are similar, as in the case of the other control strategies.

Table 3. Parameters.

	Parameter	**Value**
NPC Module		
V_{dc}	DC-Link Voltage	600 [V]
V_{ces}	Blocking Voltage	650 [V]
I_{cnom}	Collector nominal current	300 [A]
$V_{ce,sat}$	Collector emitter saturation voltage	1.55 [V]
$R_{thi,jc}$	IGBT thermal resistance junction to case	0.16 [K/W]
$R_{thi,ch}$	IGBT thermal resistance case to heat-sink	0.063 [K/W]
$R_{thd,jc}$	Diode thermal resistance junction to case	0.32 [K/W]
$R_{thd,ch}$	Diode thermal resistance case to heat-sinkk	0.125 [K/W]
Squirrel Cage Induction Motor		
P_n	Nominal Power	15 [kW]
V_s	Nominal Voltage	400 [$V_{LL,rms}$]
$n_{r,nom}$	Rated speed	1460 [RPM]
I_n	Nominal current	30 [A_{rms}]
T_n	Nominal torque	98 [Nm]
p	Pole Pairs	2
R_s	Stator Resistance	0.2147 [Ω]
$L_{\sigma s}$	Stator Leakage Inductance	0.991 [mH]
R_r	Rotor Resistance	0.2205 [Ω]
$L_{\sigma r}$	Rotor Leakage Inductance	0.991 [mH]
L_m	Magnetizing Inductance	64.19 [mH]
Real-time RT-Box		
T_s	Sampling Time	10 [μs]

In Figure 22, the relationship between conduction and switching losses and the load torque of the induction machine is depicted. The conduction losses, illustrated in Figure 22a, exhibit a direct dependence on the load current, resulting in an expected increase in losses as the torque rises. It is evident that the growth of conduction losses is more exponential in the case of DTC compared to the other control strategies, that exhibit a more linear behavior. This fact indicates a stronger correlation between DTC and load torque in terms of conduction losses. For SC, FOC, and MPC, with restricted switching frequency, conduction losses are more linear and quite similar to each other.

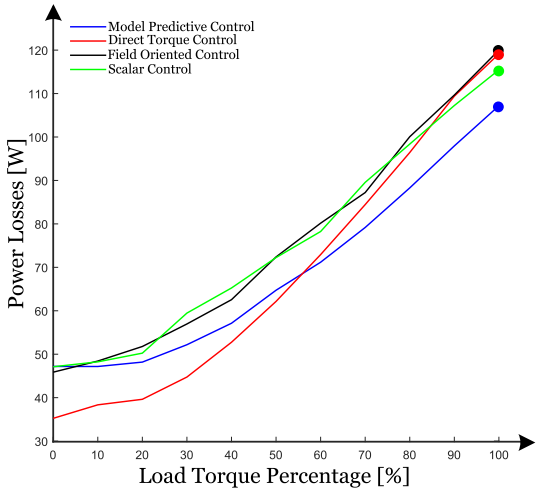

(**a**) Conduction losses in the NPC converter

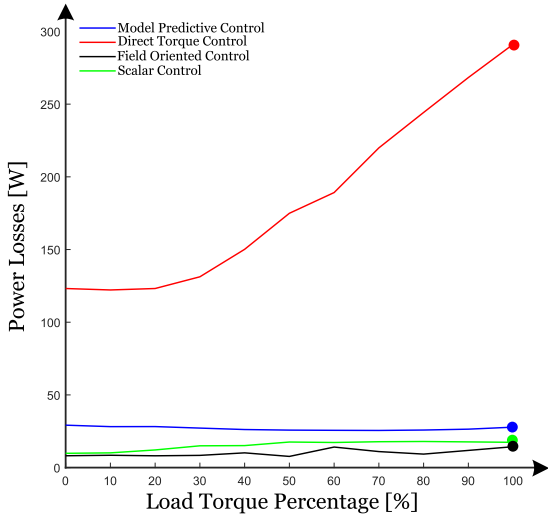

(**b**) Switching losses in the NPC converter

Figure 22. Power losses v/s load torque in an NPC inverter according to drive controls.

The behavior of switching losses, on the other hand, is shown in Figure 22b. As presented, SC, FOC, and MPC with switching frequency limitation, there is nearly no increase in switching losses with load torque demand. This is due to the fact that the switching losses primarily depend on the switching frequency and are less influenced by the load. On the other hand, as observed in the DTC scheme, switching losses experience a linear growth with the increasing load torque. As the torque increases, the commutation process becomes faster due to the actuation of the hysteresis controllers and the switching state design.

Figure 23 shows the relationship between total power losses and the switching frequency of the sPWM modulation technique for the SC and FOC schemes. Such analysis

cannot be conducted for the MPC and DTC schemes because their working principle is independent of the switching frequency (unless the Notch filter implemented within the cost function of MPC is adapted). As shown, losses increase linearly as the frequency increases, which is consistent with Equation (2). As presented in Figure 23, SC and FOC control schemes exhibit comparable switching losses at low switching frequencies, hence close to 5 kHz; for switching frequencies above 5 kHz, FOC exhibit a better performance in terms of switching losses compared to SC.

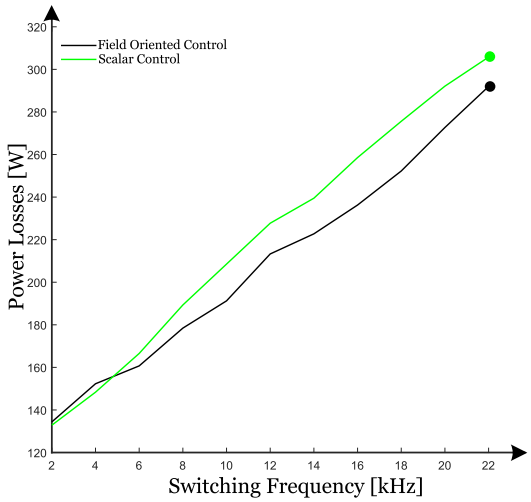

Figure 23. Total power losses v/s switching frequency in an NPC inverter according to drive controls with a nominal torque.

As stated previously, total losses are not symmetrically distributed within the power semiconductors in the 3L-NPC topology. This fact is due to the effect of the clamping diodes; thus, total losses on S_1 are higher than in S_2, as shown in Figure 24. Switching device S_1 is more sensitive to the switching frequency compared to S_2. Moreover, the commutation of clamping diode D_c becomes more significant as the switching frequency increases. It should be noted that there is a specific point at which the losses of the clamping diode become equal to the losses of S_2. Above this crossing frequency, losses of the clamping diode will overpass those of S_2.

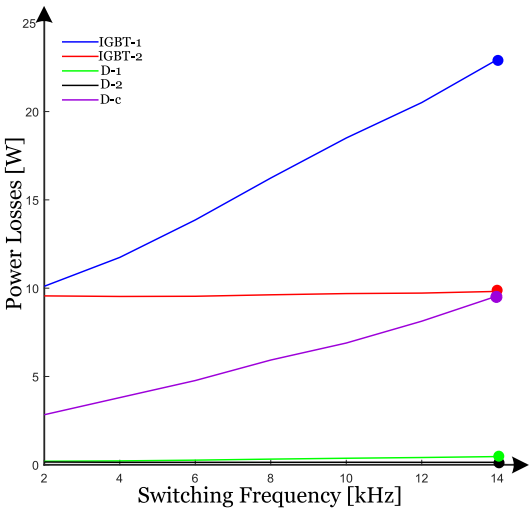

Figure 24. Power losses of each semiconductor v/s switching frequency in an NPC for an FOC scheme with a nominal torque.

The main consequence of this asymmetric distribution within the NPC converter is related to thermal stress of the power devices. Since the S_1 experiences higher losses, its operating temperature will be higher; thus, the risk of damage and failure probability increases.

7. Discussion

Table 4 shows the conduction and switching losses in the NPC topology under rated operational conditions, e.g., nominal speed and load torque. In this context, SC and FOC control schemes exhibit the lowest power losses compared to the control schemes that are not based on SPWM: MPC (with switching frequency restrictions) and DTC. Here, the difference between SC, FOC, and MPC in terms of power losses is not very significant; however, it should be noted that MPC has an additional switching constraint that has been included within the cost function.

On the other hand, the direct torque control (DTC) scheme shows the worst performance in terms of power losses compared to the other three control schemes, as presented in Figures 21 and 22 and Table 4.

Table 4. Power losses of each drive control.

	Scalar Control	**Field-Oriented Control**	**Model Predictive Control**	**Direct Torque Control**
P_{cond}	17.3879	14.3675	27.8165	119.1384
P_{sw}	115.453	120.0106	107.1836	291.134
P_t	132.841	134.3781	135.0012	410.2724
$Efficiency$	99.12%	99.1%	99.09%	97.26%

System efficiency can be evaluated as a function of the power losses of the converter compared to its rated power. In this context, the DTC scheme presents the lowest efficiency, while the other three control schemes exhibit a better performance and are very close to each other in terms of efficiency, as presented in Table 4. In Figure 25, the efficiency is plotted as a function of the load torque and the switching frequency. Scalar and field-oriented control schemes show better performance compared to the other studied control strategies, exhibiting an almost constant efficiency across all loading conditions. On the other hand, the direct torque control (DTC) scheme consistently exhibits lower efficiency, consistent with its overall performance trend. The model predictive control (MPC) scheme shows more variation in efficiency compared to the other control schemes: at higher loads, the efficiency increases, but at a lower loading condition, the efficiency starts to decrease exponentially. This behavior is similar to that of the DTC scheme on the low load operating region due to the switching frequency constraint on the cost function.

Figure 25b shows the dependency of the efficiency related to the switching frequency, in the case of SC and FOC. As the frequency increases, switching losses become more relevant compared to conduction losses. In this context, as presented in the same figure, the field-oriented control scheme presents better performance compared to scalar control, as the switching frequency increases. This results highlights the importance of controlling the switching frequency; thus, operating beyond the critical frequency f_{cri} can have a significant impact on system efficiency.

In this same context, with reference to SC and FOC, in Figure 26, a relationship between the load torque, switching frequency, and total losses in the NPC inverter is presented, for both the scalar and field-oriented control schemes. It is observed that there is a direct relationship between power losses and both the load torque and the frequency of the PWM modulation. The behavior of both control schemes appears to be similar for power ratings

below a 60% load. However, above the 60% load, FOC presents better performance in terms of losses compared to SC.

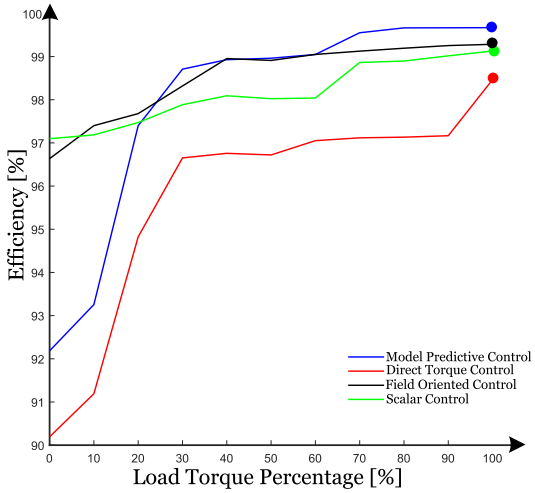

(**a**) Efficiency in function the load torque

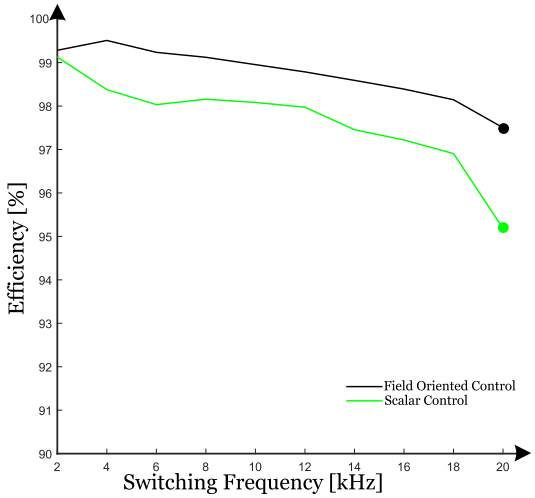

(**b**) Efficiency in function the switching frequency

Figure 25. System efficiency in function of the switching frequency and the load torque for each control scheme.

It should be noted that switching and conduction losses are the origin of high operating temperatures, decreasing the efficiency of heat dissipation. During the common operation of the converter, temperature oscillations occur, causing contractions and expansions of the various module materials, and leading to the thermal stress effect. High thermal stress results in an increase in thermal resistance, reducing the heat dissipation capacity and increasing the junction temperature until eventual failure. In other words, a high variability in the operating temperatures causes damage to the semiconductor, leading to failure in the medium or long term [24–27].

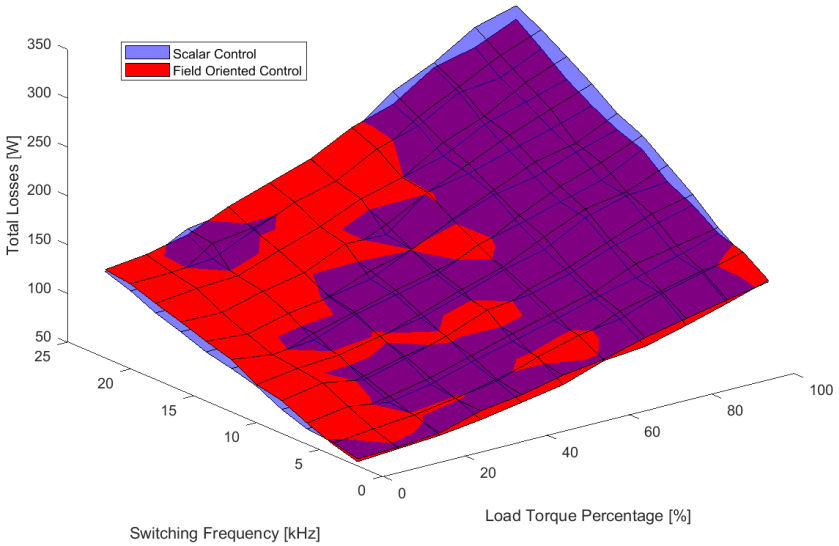

Figure 26. Total power losses in function of the switching frequency and the load torque.

8. Conclusions

Switching losses are a key component in the total efficiency, which are highly dependent on the modulation strategy. In the case of scalar control and field-oriented control schemes, both are based on the use of linear controllers and a pulsed modulation (PWM) scheme, with a fixed carrier frequency, so switching losses are fixed to the PWM frequency. In this context, the efficiency of both control schemes appear to be similar for power ratings below the 60% load. However, above the 60% load, FOC presents a better performance in terms of losses compared to SC.

In model predictive control (MPC) and direct torque control (DTC) schemes, because of their working principle, the switching frequency and sequence of power devices is variable, directly impacting higher switching and conduction losses, reducing efficiency. In the case of MPC, the inclusion of a Notch filter within the cost function enables the control strategy to have a close similar behavior, in terms of efficiency, to the PWM-based control schemes: scalar and field-oriented control. However, there is extra difficulty in designing the Notch filter. On the other hand, this switching frequency constraint cannot be included within the direct torque control formulation. Moreover, losses are very sensitive to the design of the switching table in DTC.

In the selection of a control strategy, the switching frequency for a given operation load pattern becomes a very relevant matter in terms of the impact of the system efficiency and, moreover, for particularities of the 3L-NPC topology, where losses are unequally distributed in the active switching devices; hence, some devices are more susceptible to failure.

This work has presented an analysis of the total losses in an NPC-based electric drive for classical control schemes, such as VF, FOC, DTC, and MPC, under different load conditions and switching frequencies and their relationship to the selection of the most suitable control strategy and switching frequency for a given operation load pattern, in terms of the impact of the system efficiency. Moreover, for particularities of the 3L-NPC topology, where the losses are unequally distributed in the active switching devices, this work offers an analysis of the life span expectations of these switching devices, as a function of their thermal stress.

Author Contributions: Conceptualization, C.A.R. and M.P.; formal analysis, C.A.R., M.P. and G.M.-A.; funding acquisition, C.A.R. and G.M.-A.; investigation, C.R, M.P., G.M.-A. and V.R.G.-D.; methodology, C.A.R., M.P., G.M.-A. and V.R.G.-D.; resources, C.A.R. and G.M.-A.; software, M.P.; validation, C.A.R., M.P., G.M.-A. and V.R.G.-D.; visualization, C.A.R. and M.P.; writing—original draft preparation, C.A.R., M.P., G.M.-A. and V.R.G.-D.; writing—review and editing, C.A.R., M.P., G.M.-A. and V.R.G.-D. All authors have read and agreed to the published version of the manuscript.

Funding: DI Iniciación 039.487/2024, Pontificia Universidad Católica de Valparaíso.

Data Availability Statement: The original contributions presented in this study are included in the article material. Further inquiries can be directed to the corresponding author.

Acknowledgments: The authors acknowledge the support provided by the VINCI-DI of Pontificia Universidad Católica de Valparaíso, through the project: DI Iniciación 039.487/2024.

Conflicts of Interest: The authors declare no conflicts of interest.

Abbreviations

The following abbreviations are used in this manuscript:

2L-VSC	two-level voltage source converter
3L-NPC	three-level NPC
DTC	direct torque control
DRFO	direct reference frame orientation
FOC	field-oriented control
IM	induction machine
LS-PWM	level-shifted PWM
MPC	model predictive control
M-VSC	multilevel voltage source converter
NPC	neutral point clamped
PWM	pulse width modulation
SC	scalar control
SPWM	sinusoidal pulse width modulation
SVM	space vector modulation
THD	total harmonic distortion

References

1. Pérez, J.R. *Predictive Control of Power Converters and Electrical Drives*; Wiley: Hoboken, NJ, USA, 2012; p. 399.
2. Sul, S.K. *Control of Electric Machine Drive System*; Wiley-IEEE: Piscataway, NJ, USA, 2011; p. 399.
3. Wu, B.; Narimani, M. *High-Power Converters and AC Drives*; Wiley-Interscience: Hoboken, NJ, USA, 2017; p. 480.
4. Alemi, P.; Lee, D.C. Power loss comparison in two- and three-level PWM converters. In Proceedings of the 8th International Conference on Power Electronics—ECCE Asia, Jeju, Republic of Korea, 30 May–3 June 2011; pp. 1452–1457. [CrossRef]
5. Dieckerhoff, S.; Bernet, S.; Krug, D. Power loss-oriented evaluation of high voltage IGBTs and multilevel converters in transformerless traction applications. *IEEE Trans. Power Electron.* **2005**, *20*, 1328–1336. [CrossRef]
6. Babaie, A.; Karami, B.; Abrishamifar, A. Improved equations of switching loss and conduction loss in SPWM multilevel inverters. In Proceedings of the 2016 7th Power Electronics and Drive Systems Technologies Conference (PEDSTC), Tehran, Iran, 16–18 February 2016; pp. 559–564. [CrossRef]
7. Andler, D.; Kouro, S.; Perez, M.; Rodriguez, J.; Wu, B. Switching loss analysis of modulation methods used in neutral point clamped converters. In Proceedings of the 2009 IEEE Energy Conversion Congress and Exposition, San Jose, CA, USA, 20–24 September 2009; pp. 2565–2571. [CrossRef]
8. Kim, T.J.; Kang, D.W.; Lee, Y.H.; Hyun, D.S. The analysis of conduction and switching losses in multi-level inverter system. In Proceedings of the 2001 IEEE 32nd Annual Power Electronics Specialists Conference (IEEE Cat. No.01CH37230), Vancouver, BC, Canada, 17–21 June 2001; Volume 3, pp. 1363–1368. [CrossRef]
9. Gervasio, F.; Mastromauro, R.A.; Liserre, M. Power losses analysis of two-levels and three-levels PWM inverters handling reactive power. In Proceedings of the 2015 IEEE International Conference on Industrial Technology (ICIT), Seville, Spain, 17–19 March 2015; pp. 1123–1128. [CrossRef]

10. Artal-Sevil, J.S.; Lujano-Rojas, J.M.; Bernal-Ruiz, C.; Gorrachategui, I.S. Analysis of Power Losses in a Three-Phase Inverter 3L-NPC. Comparison with different PWM Modulation Techniques. In Proceedings of the 2018 XIII Technologies Applied to Electronics Teaching Conference (TAEE), La Laguna, Spain, 20–22 June 2018; pp. 1–9. [CrossRef]
11. Nabae, A.; Takahashi, I.; Akagi, H. A New Neutral-Point-Clamped PWM Inverter. *IEEE Trans. Ind. Appl.* **1981**, *IA-17*, 518–523. [CrossRef]
12. Kouro, S.; Malinowski, M.; Gopakumar, K.; Pou, J.; Franquelo, L.G.; Wu, B.; Rodriguez, J.; Pérez, M.A.; Leon, J.I. Recent Advances and Industrial Applications of Multilevel Converters. *IEEE Trans. Ind. Electron.* **2010**, *57*, 2553–2580. [CrossRef]
13. Kim, D.; Yamamoto, Y.; Nagao, S.; Wakasugi, N.; Chen, C.; Suganuma, K. Measurement of Heat Dissipation and Thermal-Stability of Power Modules on DBC Substrates with Various Ceramics by SiC Micro-Heater Chip System and Ag Sinter Joining. *Micromachines* **2019**, *10*, 745. [CrossRef] [PubMed]
14. Infineon: Semiconductors and System Solutions 2023. Available online: https://www.infineon.com/ (accessed on 20 June 2024).
15. Kazmierkowski, M.P. Electric Motor Drives: Modeling, Analysis and Control, R. Krishan, Prentice-Hall, Upper Saddle River, NJ, 2001, xxviii + 626 pp. ISBN 0-13-0910147. *Int. J. Robust Nonlinear Control* **2004**, *14*, 767–769. [CrossRef]
16. Wu, B.; Narimani, M. Control of Induction Motor Drives. In *High-Power Converters and AC Drives*; Wiley: Hoboken, NJ, USA, 2017; pp. 321–352. [CrossRef]
17. Hakami, S.S.; Alsofyani, I.M.; Lee, K.B. Direct Torque Control of IM Fed by 3L-NPC Inverter with Simple Flux Regulation Technique. In Proceedings of the 2019 IEEE Student Conference on Electric Machines and Systems (SCEMS 2019), Busan, Republic of Korea, 1–3 November 2019; pp. 1–6. [CrossRef]
18. Young, H.A.; Marin, V.A.; Pesce, C.; Rodriguez, J. Simple Finite-Control-Set Model Predictive Control of Grid-Forming Inverters with LCL Filters. *IEEE Access* **2020**, *8*, 81246–81256. [CrossRef]
19. Cataldo, P.; Jara, W.; Riedemann, J.; Pesce, C.; Andrade, I.; Pena, R. A Predictive Current Control Strategy for a Medium-Voltage Open-End Winding Machine Drive. *Electronics* **2023**, *12*, 1070. [CrossRef]
20. Cortes, P.; Rodriguez, J.; Quevedo, D.E.; Silva, C. Predictive Current Control Strategy with Imposed Load Current Spectrum. *IEEE Trans. Power Electron.* **2008**, *23*, 612–618. [CrossRef]
21. Wolbank, T.M.; Stumberger, R.; Lechner, A.; Machl, J. Novel approach of constant switching-frequency inverter control with optimum current transient response. In Proceedings of the SPEEDAM 2010, Pisa, Italy, 14–16 June 2010; pp. 803–808. [CrossRef]
22. Rivera, M.; Kouro, S.; Rodriguez, J.; Wu, B.; Yaramasu, V.; Espinoza, J.; Melila, P. Predictive current control in a current source inverter operating with low switching frequency. In Proceedings of the 4th International Conference on Power Engineering, Energy and Electrical Drives, Istanbul, Turkey, 13–17 May 2013; pp. 334–339. [CrossRef]
23. Aguirre, M.; Kouro, S.; Rojas, C.A.; Rodriguez, J.; Leon, J.I. Switching Frequency Regulation for FCS-MPC Based on a Period Control Approach. *IEEE Trans. Ind. Electron.* **2018**, *65*, 5764–5773. [CrossRef]
24. Musallam, M.; Johnson, C.M.; Yin, C.; Lu, H.; Bailey, C. In-service life consumption estimation in power modules. In Proceedings of the 2008 13th International Power Electronics and Motion Control Conference, Poznan, Poland, 1–3 September 2008; pp. 76–83. [CrossRef]
25. Musallam, M.; Johnson, C.M.; Yin, C.; Bailey, C.; Mermet-Guyennet, M. Real-time life consumption power modules prognosis using on-line rainflow algorithm in metro applications. In Proceedings of the 2010 IEEE Energy Conversion Congress and Exposition, Atlanta, GA, USA, 12–16 September 2010; pp. 970–977. [CrossRef]
26. Musallam, M.; Johnson, C.M. An Efficient Implementation of the Rainflow Counting Algorithm for Life Consumption Estimation. *IEEE Trans. Reliab.* **2012**, *61*, 978–986. [CrossRef]
27. Huang, H.; Mawby, P.A. A Lifetime Estimation Technique for Voltage Source Inverters. *IEEE Trans. Power Electron.* **2013**, *28*, 4113–4119. [CrossRef]

Disclaimer/Publisher's Note: The statements, opinions and data contained in all publications are solely those of the individual author(s) and contributor(s) and not of MDPI and/or the editor(s). MDPI and/or the editor(s) disclaim responsibility for any injury to people or property resulting from any ideas, methods, instructions or products referred to in the content.